White Rose Research Online

eprints@whiterose.ac.uk
https://eprints.whiterose.ac.uk
Universities of Leeds, Sheffield and York

Deposited via The University of Sheffield.

White Rose Research Online URL for this paper:
https://eprints.whiterose.ac.uk/id/eprint/97399/

Version: Supplemental Material

Article:
Matthiesen, C., Geller, M., Schulte, C.H.H. et al. (2013) Phase-locked indistinguishable photons with synthesized waveforms from a solid-state source. Nature Communications, 4. 1600. ISSN: 2041-1723

https://doi.org/10.1038/ncomms2601

Reuse
Items deposited in White Rose Research Online are protected by copyright, with all rights reserved unless indicated otherwise. They may be downloaded and/or printed for private study, or other acts as permitted by national copyright laws. The publisher or other rights holders may allow further reproduction and re-use of the full text version. This is indicated by the licence information on the White Rose Research Online record for the item.

Takedown
If you consider content in White Rose Research Online to be in breach of UK law, please notify us by emailing eprints@whiterose.ac.uk including the URL of the record and the reason for the withdrawal request.

Supplementary information for "Phase-locked indistinguishable photons with synthesized waveforms from a solid-state source"

Clemens Matthiesen[1], Martin Geller[1,2], Carsten H. H. Schulte[1], Claire Le Gall[1], Jack Hansom[1], Zhengyong Li[3], Maxime Hugues[4], Edmund Clarke[4] & Mete Atatüre[1]

[1]*Cavendish Laboratory, University of Cambridge, Cambridge CB3 0HE, United Kingdom*

[2]*Fakultät für Physik and CENIDE, Universität Duisburg-Essen, Duisburg 47048, Germany*

[3]*Key Laboratory of Luminescence and Optical Information of Ministry of Education, Beijing Jiaotong University, Beijing 100044, China*

[4]*EPSRC National Centre for III-V Technologies, University of Sheffield, Sheffield, S1 3JD, United Kingdom*

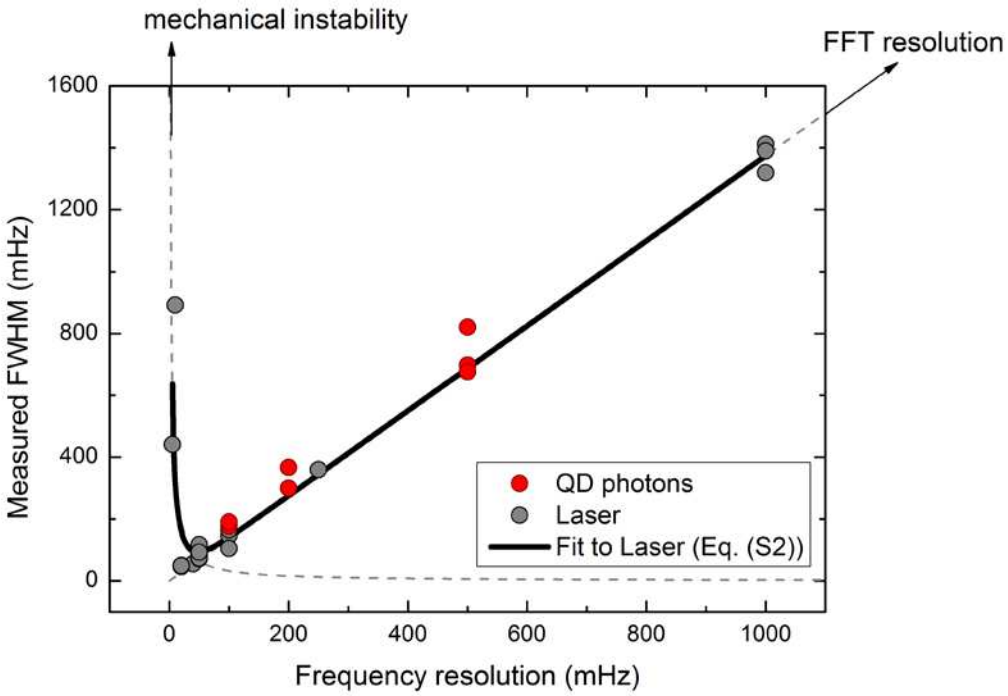

Supplementary Figure S1| Analysis of obtainable linewidth (FWHM) in heterodyning experiments with laser and QD photons as a function of FFT resolution. The phenomenological model (Eq. (S1)) fits the linewidths measured with laser photons (grey dots). The dashed grey lines represent the individual contributions of FFT resolution and mechanical instability. At very fine resolutions (<100mHz), the linewidth is limited by phase fluctuations induced by mechanical instability (vibrations) of the experimental setup. The heterodyning spectra of QD photons (red dots) show no significant broadening. The measurement of the mutual coherence time is thus limited by the response of the experimental setup.

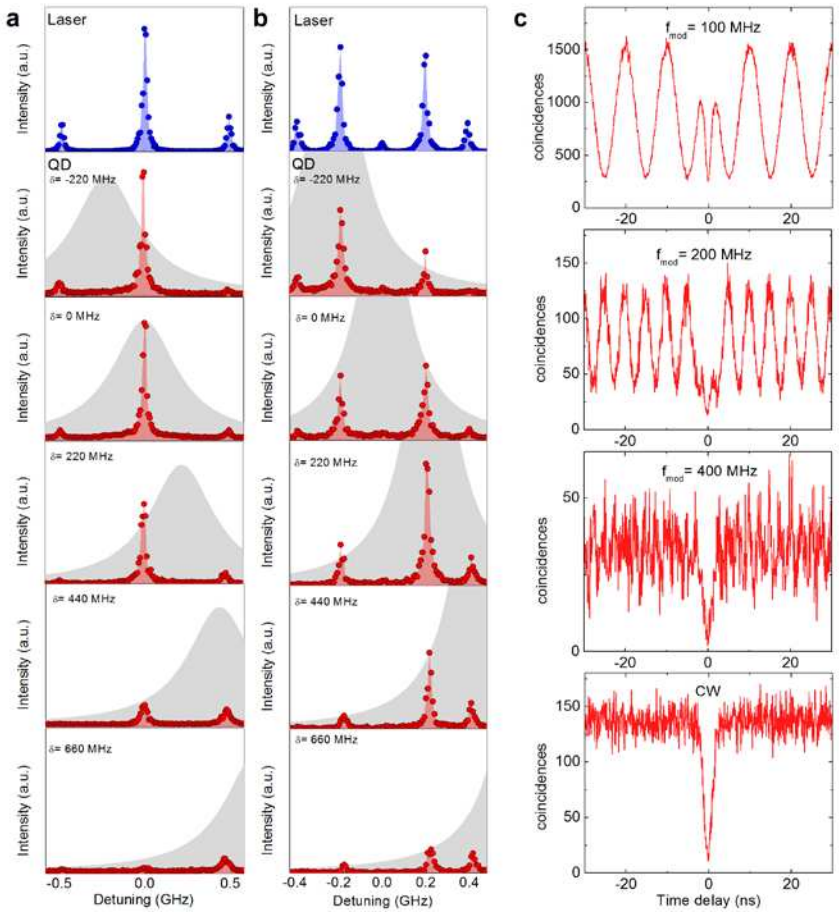

Supplementary Figure S2| Phase-locked QD RF spectra for different QD-laser frequency detuning. The narrowband single mode excitation laser is modulated by the EOM at frequencies of **a,** ν_{mod} = 200 MHz and **b,** ν_{mod} = 500 MHz, respectively. The top panels with blue dots and blue shaded areas in panels **a** and **b** show the laser spectra as measured with a Fabry-Perot interferometer (~20 MHz resolution). The lower panels with red dots display the QD RF spectra for different detuning of the QD exciton transition with respect to the laser line from δ = -220 MHz up to δ = 660 MHz. The gray shaded areas in the background are a guide to the eye giving the position and the width of the QD emission spectrum. **c,** Intensity-correlation measurements of the QD RF for a range of modulation frequencies.

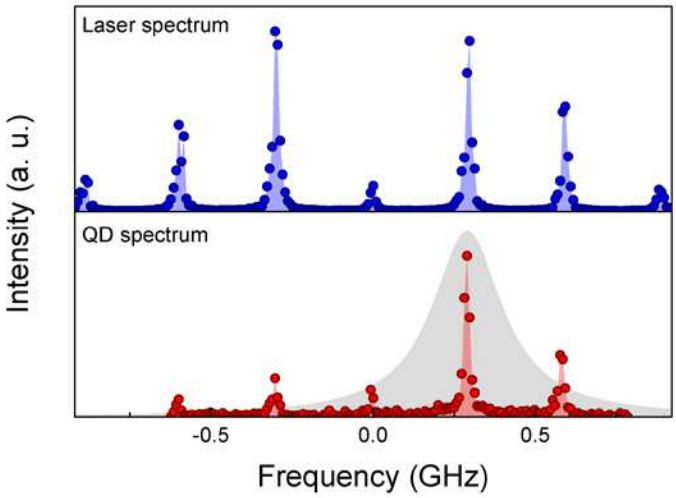

Supplementary Figure S3| Spectra for laser pulses and resulting spectra for coherent QD scattering. For the two-photon interference coherent laser pulses are created by applying electrical pulses down to 100 ps duration from an arbitrary pulse pattern generator with 10-GHz bandwidth to the EOM. An additional DC offset with feedback controls the slow drifts of the EOM operation settings. Top panel: Measured spectrum for laser pulses of ~400 ps width and a repetition rate of 300 MHz. The spacing of spectral components corresponds to the pulse repetition rate. Bottom panel: The resulting QD emission spectrum for 260-MHz detuning from the central laser frequency. Since the pulse width is significantly shorter than the QD excitonic lifetime, the amplitude of spectral components is strongly modified by the QD bandwidth.

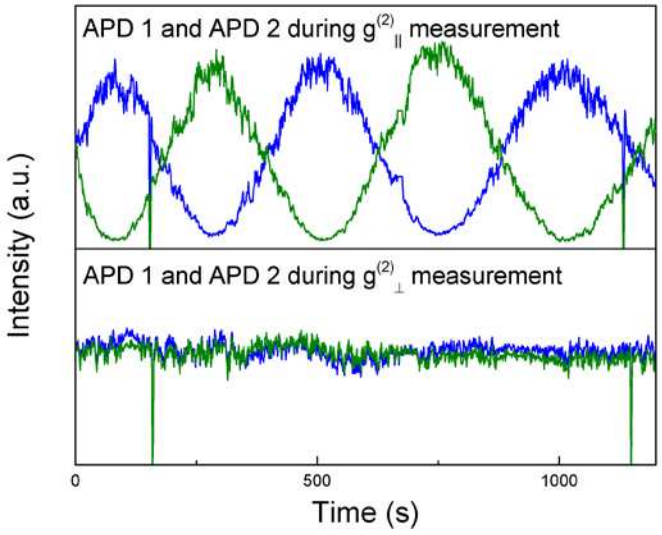

Supplementary Figure S4| First-order interference in the HOM interferometer. Detection events at both outputs of the HOM interferometer and their coincidences are recorded separately. Time traces over 1200 s for the HOM TPI from Fig. 3, main text, are presented here. Top panel: First-order interference occurs for coherent QD photons as a consequence of varying phase difference between both interferometer arms. The contrast of first-order interference quantifies the fraction of coherently scattered QD emission. Bottom panel: The time traces of detection events for photons of orthogonal polarisation stays nearly constant, as photons are distinguishable in their polarisation. The QD transition is shifted out of resonance periodically via DC Stark effect to monitor the background counts. This is visible as abrupt drops in intensity around t=200 s and t=1200 s.

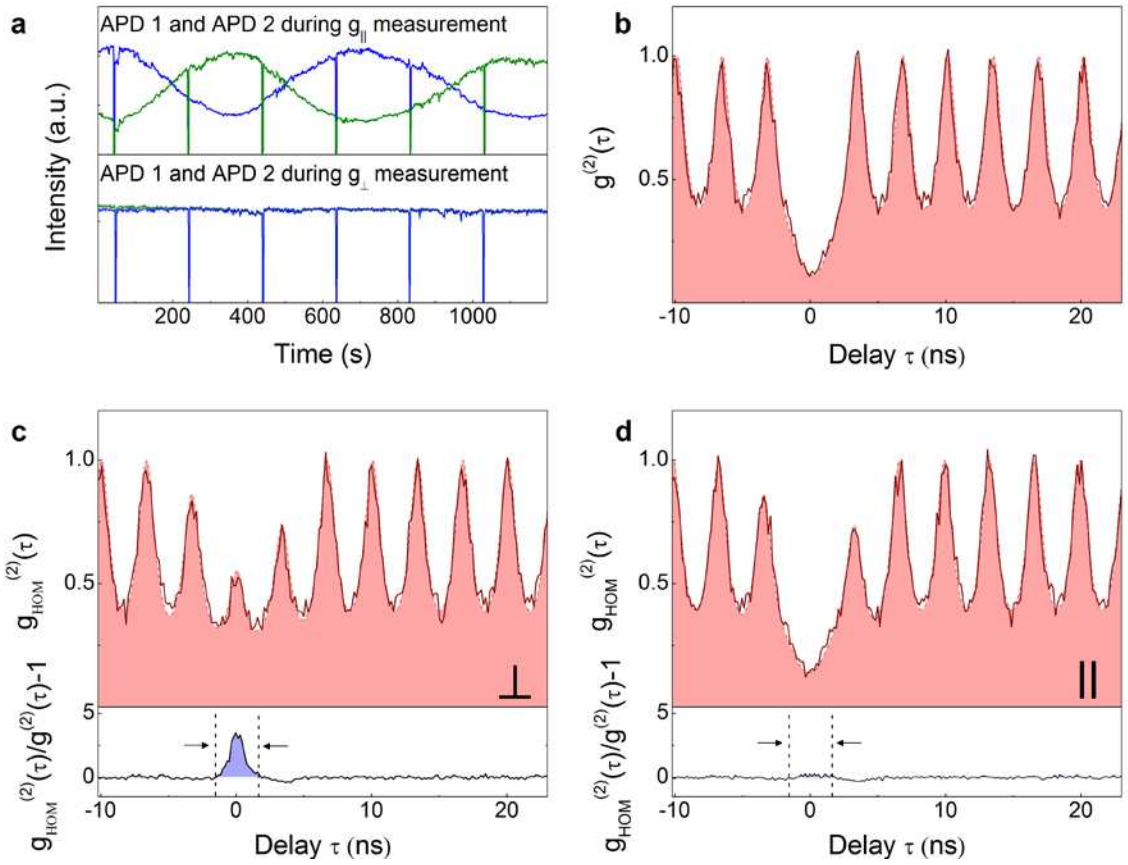

Supplementary Figure S5| Photon indistinguishability of waveform-synthesized photons. Additional measurements on HOM style TPI for higher excitation power. Panels b, c and d directly follow the presentation of Fig. 3 in the main text. The sharp intensity drops in the traces are due to the periodic background measurement. **a**, First-order interference of QD photons during HOM style measurement (compare to Supplementary Fig. S5). The time traces put the coherent fraction of QD resonance fluorescence to $c_{\mathrm{f}} = 0.45$, which corresponds to an excitation power slightly above saturation level. **b**, Intensity autocorrelation function for QD photons. **c, d** Two-photon interference (TPI) measurements for photons of orthogonal (**c**) and parallel (**d**) polarisation. The bottom panels display the normalized differences to the intensity autocorrelation in b, respectively. The lack of TPI for orthogonally polarized photons in c gives rise to coincidences at zero time delay, yielding a peak in the bottom panel. For photons of parallel polarization, the absence of coincidences around zero time delay reflects successful TPI in d. The ratio of the areas in the bottom panels yields a raw TPI contrast of 0.923 ± 0.016.

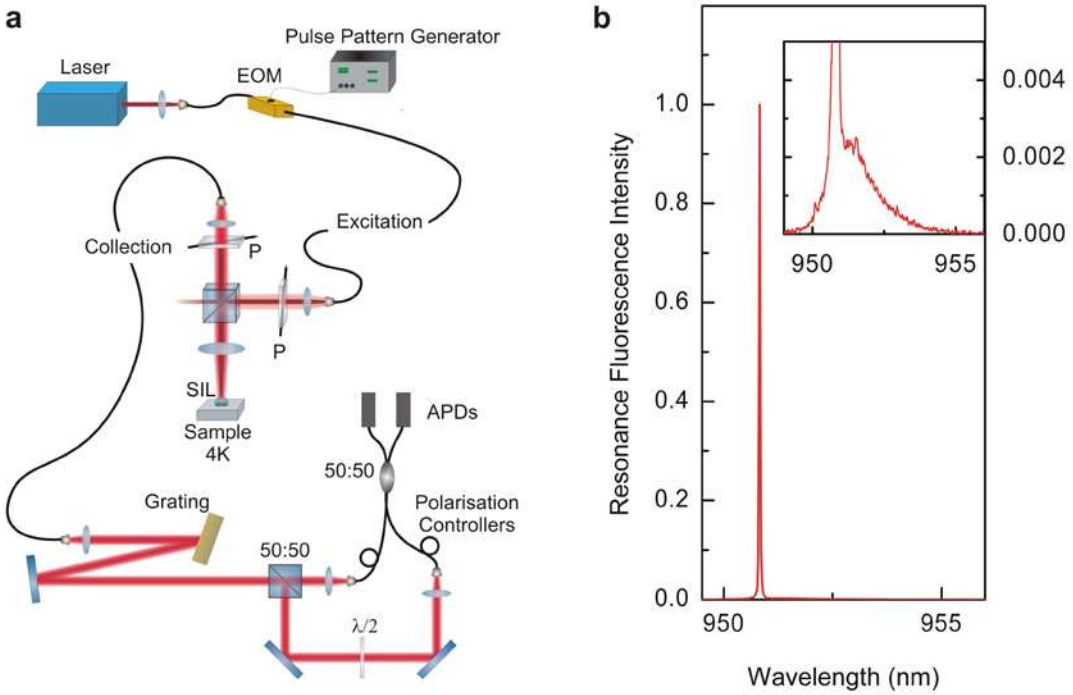

Supplementary Figure S6| Phonon sideband filtering. a, Schematics of the setup used to realize two-photon interference (TPI), which includes an electro-optical modulator (EOM), linear polarisers (P), a solid immersion lens (SIL), two nonpolarising beamsplitters (50:50), a half-wave plate ($\lambda/2$) and two single photon detectors (APDs). The excitation pulse generation is shown at the top, the confocal microscope in dark field detection mode in the middle and a filtering setup followed by the Hong-Ou-Mandel (HOM) interferometer at the bottom. A 1600 gr/mm grating acting as a bandpass filter (bandwidth when coupling back into single mode fibres of ~50 GHz) efficiently removes the phonon sideband, but preserves the spectrum of the zero-phonon line. **b,** Resonance fluorescence spectrum (around 12-GHz pixel resolution). The spectrum is normalized to the peak intensity. A zoom-in at the base of the luminescence peak (see inset) reveals the phonon-assisted scattering sideband, which represents 12% of the total QD emission. The contribution of the phonon sideband defines a maximum achievable contrast of $\left(0.88^2\right) \sim 0.77$ for TPI measurements without spectral filtering. Experimentally, we measure a raw contrast of 0.7 for this case. We note that QDs grown under different conditions show phonon sideband contributions as low as 5% of total fluorescence[37].

Supplementary Note 1

Contributions to QD heterodyne linewidth. As mentioned in the main text, the measured linewidth $\Delta\nu_{\mathrm{FWHM}}$ is limited by the system response at a given FFT resolution. For resolutions >100 mHz, $\Delta\nu_{\mathrm{FWHM}}$ is governed by the FFT resolution f_{res}. At finer resolution, i.e. longer integration times $t_{\mathrm{int}} = 1/f_{\mathrm{res}}$, mechanical vibrations and other sources of phase fluctuations, i.e. spectral wandering of the transition frequency, are more likely to perturb the measurement and additionally broaden the line. Assuming this additional broadening to be proportional to integration time yields a total convolved linewidth of

$$\Delta\nu_{\mathrm{FWHM}} = A\cdot\sqrt{{f_{\mathrm{res}}}^2 + \left(B\cdot t_{\mathrm{int}}\right)^2} = A\cdot\sqrt{{f_{\mathrm{res}}}^2 + \left(\frac{B}{f_{\mathrm{res}}}\right)^2}\,, \qquad \text{(S1)}$$

where *A* and *B* are fit parameters. Supplementary Figure S1 shows the linewidths obtained with laser photons as strong signal field (grey dots) at different FFT resolutions using the same setup as in Fig. 1 of the main text. Comparing these measurements with linewidths obtained with QD photons (red dots) illustrates that the obtained mutual coherence is limited by the system response. In particular, spectral wandering does not lead to additional phase fluctuations and can therefore be neglected on the timescale of the integration time. In all heterodyning experiments the delay between signal and local oscillator beam due to beam path difference amounts to ~100 ns, which is small compared to the laser coherence time.

Supplementary Note 2

Photon waveform synthesis: temporal and spectral domain. In Supplementary Figure S2 we present supplementary data which complement the results presented in Fig. 2 of the main text, showing how the spectral and temporal properties of a laser are encoded on the single photons coherently emitted by the quantum dot. Here, the EOM is driven by a sine wave, as discussed above. The amplitude of the sine-wave determines the shape of the waveform and the height of the components in the laser spectrum while the driving frequency determines the separation of the spectral components. In Supplementary Fig. S2a, the waveform of the laser is similar to that displayed in Fig. 2a of the main text, but with a modulation of 500 MHz, while in Supplementary Fig. S2b, the waveform of the laser is identical to that in Fig. 2c of the main

text. The corresponding laser spectra are displayed as blue circles, while the spectra of the QD photons are displayed in red circles. The detuning between the QD transition and the central frequency component of the laser is controlled by the gate bias voltage via the DC Stark effect. As a guide to eye the QD scattering cross-section (grey shaded area) is superimposed to indicate the expected scaling of the laser spectral components for the QD photons.

In the weak excitation power limit the QD spectrum is expected to be a product of the input spectrum $S_{\text{laser}}(\omega)$ with the QD scattering cross-section. This can be expressed as $S_{\text{QD}}(\omega) \sim \frac{S_{\text{laser}}(\omega)}{(1/2T_1)^2 + (\omega - \omega_{\text{transition}})}$, where $\omega_{\text{transition}}$ is the frequency of the QD resonance. For stronger excitation power, this picture is complicated by the dynamic stark shift, and even for an ideal two-level system, an exploration of the theory reveals nontrivial behaviour[38].

Finally, the effects of spectral wandering have to be included. The measurement time for the Fabry-Perot scans (10^3 s for the scans shown in Fig 2) is much longer than the time-scale on which spectral wandering occurs. Therefore, the spectrum of the QD is further broadened by 100 MHz due to long timescale (seconds) spectral wandering. The temporal profile of the QD photons is a convolution of the laser waveform and the response function of the QD. Supplementary Figure S2c presents intensity-correlation measurements on QD photons for a range of EOM modulation frequencies. The periodic temporal pattern of the excitation laser is seen clearly for modulation frequencies within the bandwidth of the QD transition, while for high modulation frequencies the QD photons can not follow the temporal pattern of the laser and the oscillatory features in the intensity-correlation measurements wash out. We note that for all modulation frequencies the antibunched nature of the QD photons at zero time delay is preserved.

Supplementary Note 3

First-order interference in TPI measurements. Individual detection events on both avalanche photodiodes (APDs) at the output ports of the fibre beamsplitter are monitored throughout the correlation measurements. Time traces over 1200 s for the HOM TPI from Fig. 3, main text, are shown in Supplementary Figure S4. For photons with parallel polarisation (top panel) we observe first-order interference as the phase difference between both interferometer arms changes over time due to mechanical wandering and slight changes in ambient temperature. For the 1200-s data presented in Supplementary Fig. S4 this drift is monotonic.

While the rate of two-photon detection events depends on the product of intensities in each interferometer output and is modified by the presence of first-order interference, the process of TPI (coincidence detections around zero time delay) still takes place. The contrast of first-order interference quantifies the fraction of coherently scattered QD emission c_{f}, which is $c_{\mathrm{f}} = 0.92$ for the data in Fig. 3. The time traces of detection events for photons of orthogonal polarisation (bottom panel of Supplementary Fig. S4) stays roughly constant, as no interference occurs. For the purpose of data calibration the QD transition was periodically shifted out of resonance with respect to the exciting laser, so that the background counts due to detector dark counts and laser leakage were recorded. This is visible as sharp drops in intensity in Supplementary Fig. S4. Care was taken to keep the background level below 1% in all measurements.

Supplementary Note 4

Evaluation of photon indistinguishability. The raw contrast of the HOM style TPI constitutes a lower bound to photon wavepacket indistinguishability, as the measurement is affected by imperfections of the setup. In our case these include polarisation degradation in the single mode fibre beamsplitter and imbalance of beamsplitter coefficients. The conventional treatment of these imperfections[34,39] assumes that the photon coherence time τ_{c} is much shorter than the time delay in the interferometer, $\tau_{\mathrm{c}} << \Delta t_{\mathrm{delay}}$. The expected HOM contrast is then

$$C_{\mathrm{HOM}} = 1 - \frac{A_{\mathrm{pa}}}{A_{\mathrm{or}}} = 1 - \frac{2R_2T_2p_{\mathrm{pa}}\left(D-1\right) + R_2^2 + T_2^2}{2R_2T_2p_{\mathrm{or}}\left(D-1\right) + R_2^2 + T_2^2}, \qquad \text{(S2)}$$

where D is the distinguishability of photon pairs. Experimentally we measure the fraction $A_{\mathrm{pa}}/A_{\mathrm{or}}$ and then determine $\left(1-D\right)$, knowing the values and error estimates for all parameters involved in Eq. (S2). For the data in Fig. 3 of the main text this gives $\left(1-D\right) = 1.03 \pm 0.05$. Supplementary Figure S5 for the same parameters (except for $p_{\mathrm{pa}} = 0.99 \pm 0.01$) gives $\left(1-D\right) = 1.00 \pm 0.05$.

For coherently scattered photons the correction for the interferometer imperfections is not straightforward as their coherence time exceeds the interferometer time delay, therefore we choose to correct only for the polarisation mismatch which affects coherent and incoherent photons in the same way. The expected HOM contrast then yields

$$C_{\mathrm{HOM}} = 1 - \frac{A_{\mathrm{pa}}}{A_{\mathrm{or}}} = 1 - \frac{1 - p_{\mathrm{pa}} + Dp_{\mathrm{pa}}}{1 - p_{\mathrm{or}} + Dp_{\mathrm{or}}}. \tag{S3}$$

Using Eq. (S3), a lower bound on indistinguishability of photon pair wavepackets is obtained as $(1-D) \geq 0.96 \pm 0.04$ for Fig. 3 and $(1-D) \geq 0.94 \pm 0.04$ for Supplementary Fig. S5.

Supplementary Methods

Electro-optic waveform shaping. For the photon waveform shaping presented in Figs. 2 and 3 of the main text we employ a fibre based electro-optic intensity modulator (EOM) with a bandwidth of 5 GHz. The throughput I of the EOM as a function of applied bias V_{bias} follows

$$I\left(V_{\mathrm{bias}}\right) \sim \frac{1}{2}\cos\left(kV_{\mathrm{bias}} + \phi_{\mathrm{offset}}\right) + \frac{1}{2}, \tag{S4}$$

where constant k relates the bias voltage to a phase shift of the cosine function and $\varphi_{\mathrm{offset}}$ determines the working point of the EOM. In Fig. 2a the EOM is driven by a high purity sine wave at $\nu_{\mathrm{mod}} = 200\,\mathrm{MHz}$ with variable amplitude A. The intensity modulation of the laser is then given by

$$I\left(t\right) \sim \frac{1}{2}\cos\left(kA\sin\left(\nu_{\mathrm{mod}}t\right) + \phi_{\mathrm{offset}}\right) + \frac{1}{2}. \tag{S5}$$

Complex intensity patterns, as displayed in Fig. 2c, can be generated with $kA > \pi$. The resulting spectrum is given by the Fourier transform of the first-order correlation function of the output field of the EOM.

Supplementary References

37. Konthasinghe, K. *et al.* Coherent versus incoherent light scattering from a quantum dot. *Phys. Rev. B* **85**, 235315.

38. Newbold, M.A. & Salamo, G.J. Power spectrum of light scattered by a two-level atom in the presence of a pulse-train driving field. *Phys. Rev. A* **22** 2098-2107 (1980).

39. Patel, R. B. *et al.* Postselective Two-photon interference from a continuous nonclassical stream of photons emitted by a quantum dot. *Phys. Rev. Lett.* **100**, 207405 (2008).